ELSEVIER

Three-dimensional forward and backward modelling of diapirism: numerical approach and its applicability to the evolution of salt structures in the Pricaspian basin

Alik Ismail-Zadeh[a,b,*], Igor Tsepelev[c], Chistopher Talbot[d], Alexander Korotkii[c]

[a]*Geophysikalisches Institut, Universität Karlsruhe, Hertzstrasse 16, Karlsruhe D-76187, Germany*
[b]*International Institute of Earthquake Prediction Theory and Mathematical Geophysics,*
Russian Academy of Sciences, Warshavskoye sh. 79-2, Moscow 133556, Russia
[c]*Institute of Mathematics and Mechanics, Ural Branch, Russian Academy of Sciences, ul. S. Kovalevskoy 16,*
Yekaterinburg 620219, Russia
[d]*Department of Earth Sciences, Uppsala University, Villavägen 16, Uppsala 75236, Sweden*

Abstract

Numerical studies of ductile deformations induced by salt movements have, until now, been restricted to two-dimensional (2D) modelling of diapirism. This paper suggests a numerical approach to model the evolution of three-dimensional (3D) salt structures toward increasing maturity. This approach is also used here to restore the evolution of salt structures through successive earlier stages. The numerical methodology is applied to study several model examples. We analyse a model of salt diapirs that develop from an initial random perturbation of the interface between salt and its overburden and restore the evolved salt diapirs to their initial stages. We show that the average restoration errors are less than 1%. An evolutionary model of a 2D salt wall loaded by a 2D pile of sediments predicts a decomposition of the salt wall into 3D diapiric structures when the overburden of salt is supplied by 3D synkinematic wedge of sediments. We model salt extrusion feeding a gravity current over the depositional surface and estimate an average rate of extrusion and horizontal velocity of salt spreading. Faulting of the overburden to salt overhangs initiates new secondary diapirs, and we analyse the growth of these secondary diapirs. We also study how lateral flow effects the evolution of salt diapirs. The shape of a salt diapir can be very different if the rate of horizontal flow is much greater than the initial rate of diapiric growth solely due to gravity. We discuss the applicability of the results of the models to the evolution of Late Permian salt structures in the Pricaspian basin (Russia and Kazakhstan). These structures are distinguishable into a variety of styles representing different stages of growth: salt pillows, diapirs, giant salt massifs, 2D diapiric walls and 3D stocks complicated by large overhangs. The different sizes, shapes and maturities of salt structures in different parts of the Pricaspian basin reflect areal differences in salt thickness and loading history. Our results

* Corresponding author. Geophysikalisches Institut, Universität Karlsruhe, Hertzstrasse 16, Karlsruhe D-76187, Germany. Tel.: +49 721 6084610; fax: +49 721 71173.

E-mail addresses: alik.ismail-zadeh@gpi.uni-karlsruhe.de (A. Ismail-Zadeh), Tsepelev@imm.uran.ru (I. Tsepelev), christopher.talbot@geo.uu.se (C. Talbot), Korotkii@imm.uran.ru (I. Korotkii).

suggest that the numerical methodology can be employed to analyse the evolution of all salt structures that have upbuilt through younger ductile overburdens.

1. Introduction

Salt is so buoyant and weak compared to most other rocks with which it is found that it develops distinctive structures with a wide variety of shapes and relationships with other rocks by various combinations of gravity and lateral (tectonic) forces. The crests of passive salt bodies can stay near the sedimentation surface while their surroundings are buried (downbuilt) by other sedimentary rocks (Jackson et al., 1994). The profiles of downbuilt passive diapirs can simulate those of fir trees because they reflect the ratio of increase in diapir height relative to the rate of accumulation of the downbuilding sediments (Talbot, 1995) and lateral forces (Koyi, 1996). Salt movements can be triggered by faulting and driven by erosion and redeposition, differential loading, buoyancy and other geological processes. Many salt sequences are buried by overburdens sufficiently stiff to resist the buoyancy of the salt. Such salt will only be driven by differential loading into sharp-crested reactive-diapiric walls after the stiff overburden is weakened and thinned by faults (Vendeville and Jackson, 1992). Such reactive diapirs often rise up and out of the fault zone and thereafter can continue increasing in relief as by passive downbuilding of more sediment. Active diapirs are those that lift or displace their overburdens. Although any erosion of the crests of salt structures and deposition of surrounding overburden rocks influence their growth, diapirs with significant relief have sufficient buoyancy to rise (upbuild) through stiff overburdens (Jackson et al., 1994). The rapid deposition of denser and more viscous sediments over less dense and viscous salt results in the Rayleigh–Taylor (RT) instability. This leads to a gravity-driven single overturn of the salt layer with its denser but ductile overburden. It has been suggested that such actively upbuilt salt diapirs are comparatively rare (Jackson, 1995) but they exist (e.g., in the Great Kavir and the Pricaspian basin) and it is these that we take as our subject here.

RT overturns (Ramberg, 1968) are characterised by the rise of rocksalt through overlying and younger compacting clastic sediments that are deformed as a result. The consequent salt structures evolve through a great variety of shapes. Perturbations of the interface between salt and its denser overburden result in the overburden subsiding as salt rises owing to the density inversion.

Three principal approaches are used to treat salt diapirism: (1) analytical modelling suitable for studying the growth of small disturbances of a salt/overburden interface; (2) physical (analogue) experiments dynamically scaled to simulate deformation of overburden due to salt movements; and (3) numerical modelling of large deformations of sedimentary layers containing salt structures.

The theory of gravitational (RT) instability of layered media is well developed by Chandrasekhar (1961), Biot and Odé (1965), and Ramberg (1968). They studied the growth of small disturbances on the interfaces between layers under various assumptions, such as variable viscosity and thickness of layers, compaction of sediments, applied lateral forces and others. Talbot and Jarvis (1984) used analytical methods to study the shapes of salt diapirs extruding onto the surface. Several analytical studies have investigated the differences in growth rates between the RT instability of a viscous layered system and that of a system containing layers of different rheology (Naimark and Ismail-Zadeh, 1989; Conrad and Molnar, 1997; Ismail-Zadeh et al., 2001a, 2002).

Analytical methods are suitable for studying initial phases of growth of salt diapirs. However, such methods are inappropriate for analysing later phases of nonlinear diapiric growth. Physical experiments provide tools for modelling the complicated shapes of salt diapirs (e.g., Talbot, 1977, 1992; Talbot and Jackson, 1987; Jackson et al., 1988; Koyi, 1997). These experiments show qualitative features of diapiric growth, because quantification is often

limited by the practical difficulties in dynamic scaling of the physical parameters of the models to nature.

Two-dimensional (2D) numerical models of salt diapirism were first developed by Woidt (1978) who examined how the viscosity ratio between the salt and its overburden affects the shapes and growth rate of diapirs. Schmeling (1987) demonstrated how the dominant wavelength and the geometry of gravity overturns are influenced by the initial shape of the interface between the salt and its overburden. Römer and Neugebauer (1991) presented numerical results of modelling diapiric structures in a multilayered medium. Later, Poliakov et al. (1993a) and Naimark et al. (1998) developed numerical models of diapiric growth considering the effects of sedimentation and redistribution of sediments. van Keken et al. (1993), Poliakov et al. (1993b, 1996) and Daudré and Cloetingh (1994) introduced nonlinear rheological properties of salt and overburden into their numerical models.

Although the importance of three-dimensionality in studies of salt diapirism is widely recognised (e.g., Talbot et al., 1991), previous numerical investigations of large-amplitude diapirs have been limited to 2D studies. Two-dimensional analyses of the evolution of salt structures are not suitable for examining the complicated shapes of mature diapiric patterns. Resolving the geometry of gravity overturns requires three-dimensional (3D) modelling. Given the detail of natural examples revealed by modern 3D seismic exploration, salt tectonics now requires 3D modelling.

So far, only a few 3D numerical models of diapirs have been developed (Ismail-Zadeh et al., 2000; Kaus and Podladchikov, 2001). Ismail-Zadeh et al. (2000) analysed such typical 3D structures as deep polygonal buoyant ridges, shallow salt-stock canopies, and salt walls. Kaus and Podladchikov (2001) showed how complicated 3D diapirs developed from initial 2D perturbations of the interface between salt and its overburden.

The increasing application of 3D seismic exploration in oil and gas prospecting points to the need for vigorous efforts toward numerical modelling of the evolution of salt structures in three dimensions both forwards and backwards in time. Until now, most 2D and 3D numerical models of salt diapirism involved the forward evolution of salt structures toward increasing maturity. To understand the history of deformation in sedimentary basins due to sedimentation and salt diapirism, numerical tools are needed to restore salt structure and hence basin evolution. Recently, Ismail-Zadeh et al. (2001b) developed a numerical approach to 2D dynamic restoration of cross-section across salt structures. The approach was based on solving the inverse problem of gravitational advection. The same approach was used to model 3D RT instability backwards in time (Kaus and Podladchikov, 2001; Korotkii et al., 2002).

This paper studies the evolution of salt structures both forward and backwards in time by means of 3D numerical finite-element models. We consider the following evolutionary models: (i) salt diapirs evolved from an initially random perturbation of the interface between salt and its overburden and a restoration of the salt diapirs to their initial stages; (ii) a salt wall; (iii) a salt extrusion with a gravity current over the depositional surface; (iv) secondary diapirism; and (v) a salt diapir subject to horizontal forces.

Section 2 presents the evolution of salt structures in the Pricaspian basin. In Section 3, we formulate salt diapirism as a mathematical problem, consider various boundary conditions, and describe a numerical technique for forward and backward modeling of 3D slow viscous flow of salt and its overburden. Section 4 presents results of 3D numerical models for the evolution of salt structures. Section 5 discusses our results and their applicability to study the evolution of salt structures in the Pricaspian basin.

2. Salt structures of the Pricaspian Basin

The Pricaspian basin (Kazakhstan and Russia) is situated on the southeastern portion of the East-European platform at the northern end of the Caspian Sea (see Fig. 1). The basin is approximately 600 km across from west to east and is underlain by Late Permian salt. The thickness of the sedimentary cover is more than 20 km in the basin centre, and the volume of sediments is up to 6×10^6 km^3 or about 40% of the total sediment volume on the East-European platform (Volozh, 1991).

The basin infill is divided into three major sedimentary sequences: subsalt strata, salt, and overburden of the salt. The subsalt sequence contains Riphean through Lower Permian strata punctuated by
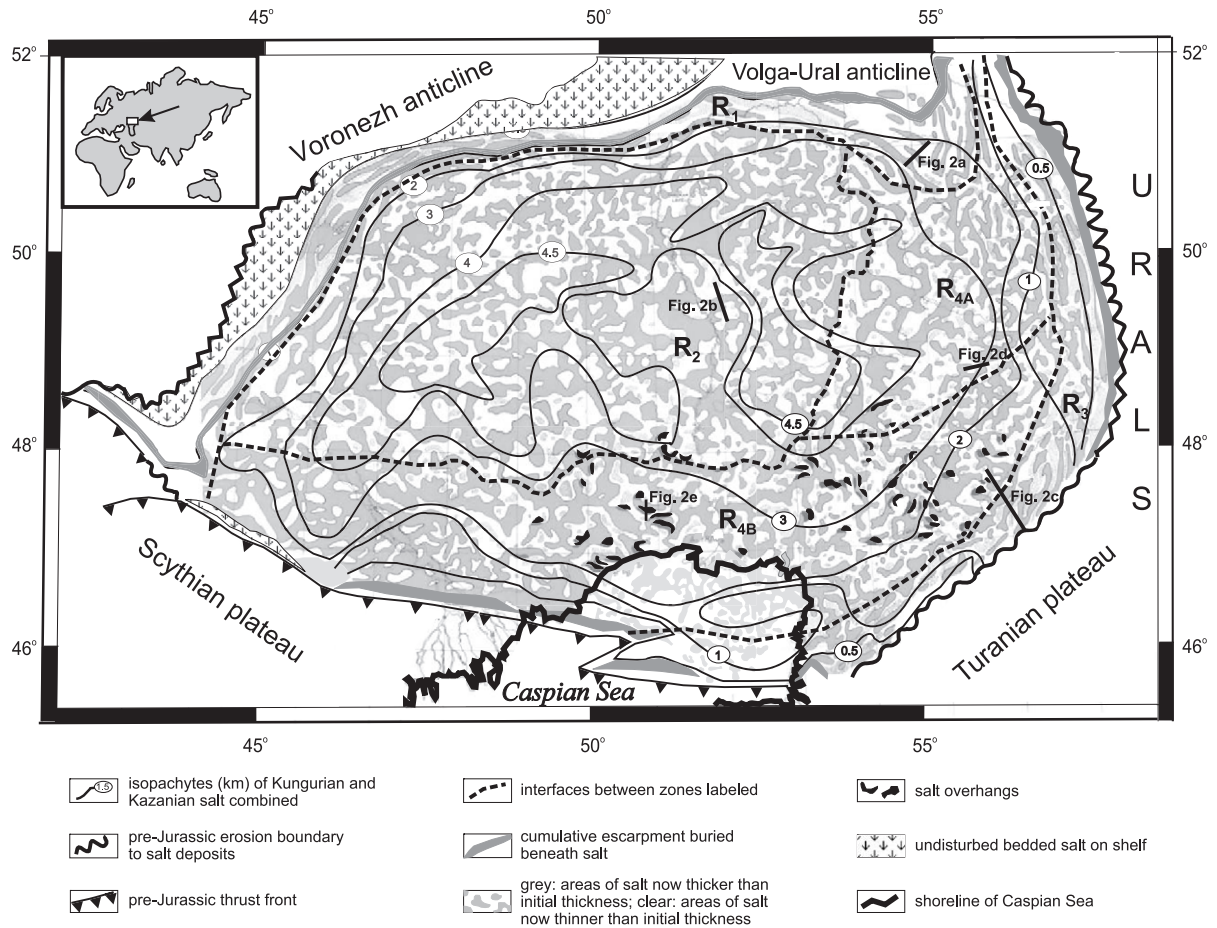
Fig. 1. Map of the Pricaspian basin showing (1) zones where the current salt structures have different shapes and (2) locations of the seismic sections illustrated. Zones: pillows of Kungurian salt (R_1), walls and domes where halokinesis involved both Kungurian and Kazanian salt (R_2), rollers, anticlines and turtlebacks of Kungurian salt (R_3), walls and domes where halokinesis involved only Kungurian salt (R_4), (A) the area of salt diapirs by the end of the Permian and (B) the area complicated by salt overhangs (modified after Ismail-Zadeh et al., 2001b).

unconformities. The subsalt sequence has a complex depositional history dominated by carbonate reefs and clastic fans. The salt sequence consists of Kungurian (~260–258 Ma) salt overlain by Kazanian (~258–252 Ma) salt which reaches a thickness of 4.5 km in the center of the basin (Fig. 1). The overburden of salt consists predominantly of terrigenous Upper Permian through Neogene strata. The overburden is divided into three structural levels by gentle unconformities at Upper Permian–Triassic, Jurassic–Miocene, and Plio-cene–Quaternary (Volozh et al., 2003).

About 1800 structures in the Pricaspian basin are attributed to movements of Permian salt. These structures are distinguishable into a variety of styles — distributed geographically (zones R_1–R_4 in Fig. 1 and Table 1) representing different stages of growth: salt pillows and immature salt structures (see zone R_1 in Fig. 1 and relevant seismic image in Fig. 2a), giant salt massifs (zone R_2 in Figs. 1 and 2b), salt rollers, anticlines, and turtlebacks (zone R_3 in Figs. 1 and 2c), and 2D diapiric walls and 3D stocks (zone R_{4A} in Figs. 1 and 2d) complicated by extensive overhangs (zone R_{4B} in Figs. 1 and 2e).

Kungurian salt remains flat-lying on shelves starved of clastic sediments along the northern and western margins of the basin and were tilted shoreward between down-to-basin faults along the narrow slopes (zone R_1, Fig. 1). The Kungurian salt was overlain by

Table 1
Summary of salt structures in the Pricaspian basin derived from Volozh et al. (2003)

Age	Zones				
	R_1	R_2	R_3	R_{4A}	R_{4B}
Late Permian Kungurian and Kazanian **Tatarian, ~252 to 248 Ma**	**Salt deposition** (~260 to 252 Ma)				
			salt pillows (~258 to 252 Ma)		
	symmetrical salt pillows and walls (*Fig. 2a*)	no salt movements	inclined salt walls	immature salt structures	no salt movements
Trias	Hiatus (~248 to 242 Ma)				
	undeformed sall walls	salt massifs (*Fig. 2b*) surrounded by smaller salt structures	salt diapirs, turtleback structures, stocks (*Fig. 2c*)	salt diapirs (*Fig. 2d*)	asymmetric salt diapirs and stocks
	Hiatus (~208 to 170 Ma)				**salt overhangs** (*Fig. 2e*)
Jurassic	reactivation of salt movements; symmetric salt diapirs, walls and stocks				
Cretaceous					
Paleocene to Pliocene	Neogene reactivation of salt movements				
					secondary salt diapirism
Pliocene	Hiatus				

Zones 1_1–R_4 are identified in Fig. 1.

Kazanian salt in the basin centre, where slow and almost continuous deposition downbuilt an unusually thick salt layer into huge massifs (zone R_2, Fig. 1). In marked contrast, salt walls and stocks were downbuilt in Permian salt by clastic sediments derived from the eastern and southeastern margins in Permian to Triassic times (zone R_3, Fig. 1). They were later influenced by the development of the Ural orogen to the east. Later, these early salt structures were starved, as their deep source layer closed to a weld. (We distinguish starved salt structures surrounded by welds from those that still have the potential for growth because their source layer has not been welded.) Gravity (not lateral forces) was the dominant influence on structures developing in the salt and its overburden almost everywhere in the basin except, perhaps, the

eastern margin of the basin where lateral shortening due to the Ural orogeny interacted with salt buoyancy.

Primary salt-withdrawal basins visible in the Upper Permian–Triassic sediments (Fig. 2) indicate early salt movements. Thereafter, zones of downbuilding salt stocks migrated basinward from the east, southeast and south margins of the basin in front of a widening zone of starved salt walls. From Triassic to Jurassic and, probably, Cretaceous times, these zones were separated by another zone of salt structures extruding Permian salt as domes with or without overhanging allochthonous sheets. Some extruded Permian salt may have been dissolved and redeposited as autochthonous salt beds (zone R_{4B} in Fig. 2e). Salt extrusion continued during a 35 My long hiatus in deposition from near end-Triassic

to Middle Jurassic. This extrusion starved a large number of basin-marginal salt structures by withdrawing salt from their deep source layer.

Subsequent deposition of shallow water Jurassic sediments was sufficiently rapid to unconformably bury the Upper Permian–Triassic sequence deformed
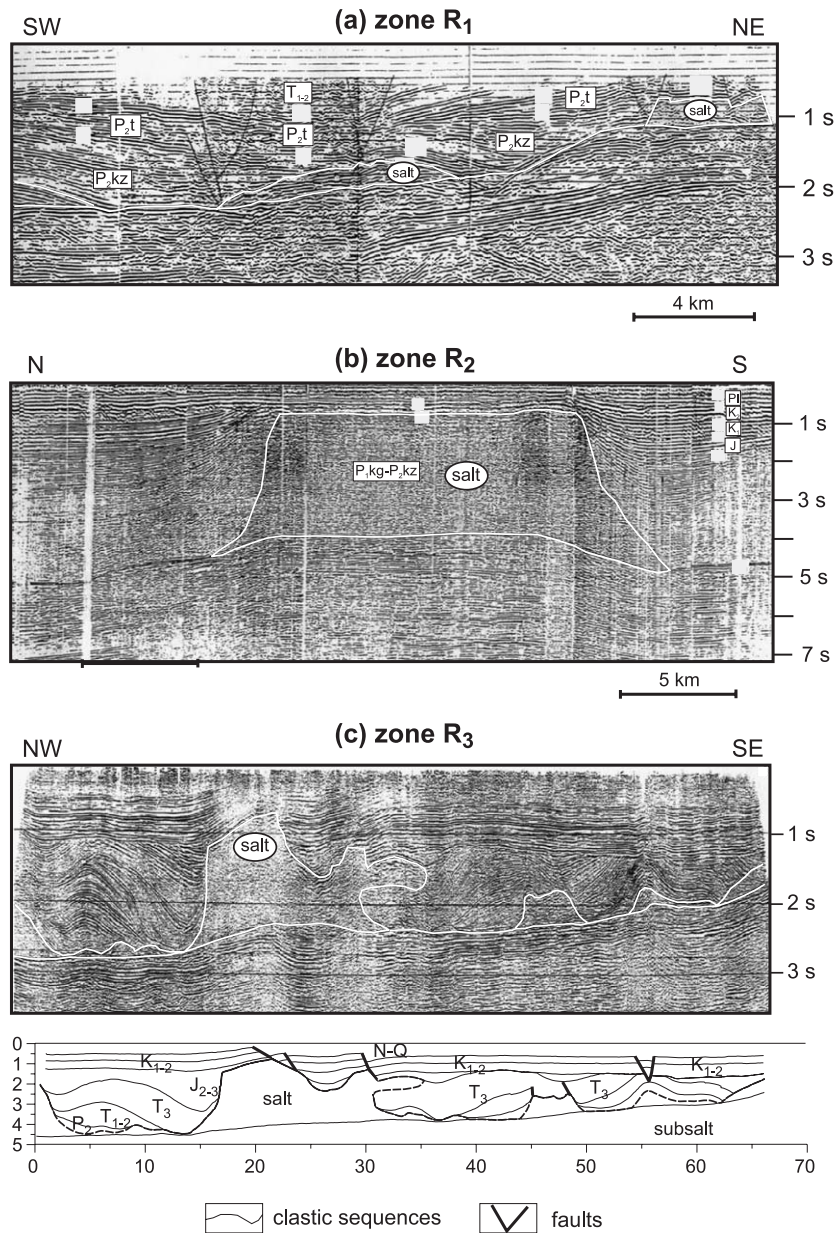

Fig. 2. (a–e) Seismic sections illustrating typical structures in salt across zones R_1–R_4 (see Fig. 1 for locations). Panel below seismic profile (c) is a depth-converted section with salt related structures. The oil field in zone R_{4B} is trapped by a sheet of allochthonous salt extruded. Notations in these sections: Lower Permian (P_1), Kungurian (P_1kg), Upper Permian (P_2), Kazanian (P_2kz), Tatarian (P_2t), Upper Permian to Lower Triassic (P_2–T_1), Triassic (T), Lower to Middle Triassic ($T_{1–2}$), Upper Triassic (T_3), Jurassic (J), Middle to Upper Jurassic ($J_{2–3}$), Lower Cretaceous (K_1), Upper Cretaceous (K_2), Paleogene (Pl), Neogene to Quaternary (N–Q) (modified after Volozh et al., 2003).
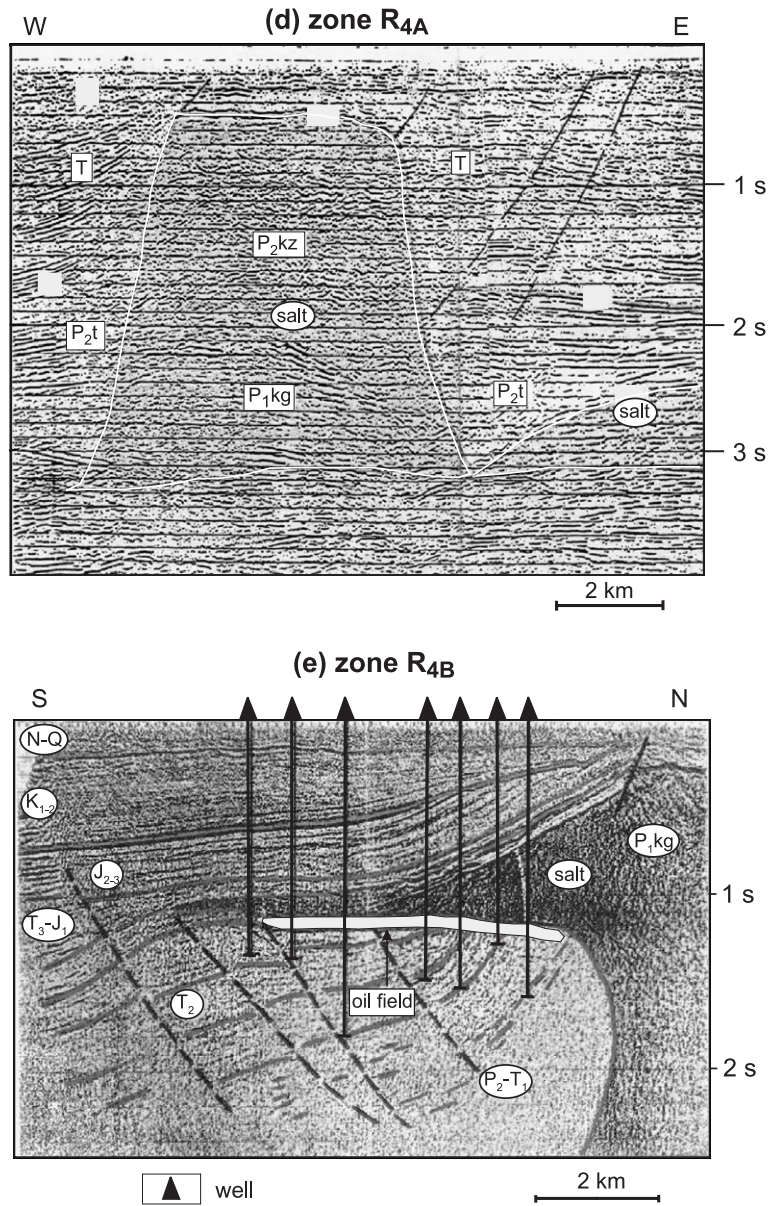
(d) zone R$_{4A}$

(e) zone R$_{4B}$

Fig. 2 (*continued*).

by salt structures, many of which had already reached the surface. But not all the deep salt supplying more basinward Permian–Triassic salt structures had been squeezed to the surface and many still-potent salt structures were reactivated by resumption of burial in the Middle Jurassic.

A pattern of polygonal graben, pointing to 5% isotropic lateral extension, connects preexisting salt structures throughout most of the basin. Volozh et al. (2003) attributed the initiation of this graben system to Early Jurassic (Cimmerian) uplift due to closure of the Palaeo–Tethys. There is no inde-

pendent evidence for either lateral extension of the Pricaspian region or uplift of the magnitude that could account for this isotropic extension (Volozh et al., 2003). Even an uplift of 2 km would result in less than 0.1% lateral extension (Price, 1966). Hence, Volozh et al. (2003) assumed that about 5% isotropic lateral shortening occurred across the polygonal normal faults and attributed this deformation to gravity having reactivated large salt structures that still had the potential for growth in smaller structures when they were buried further.

Although many salt structures continued to rise, particularly near the centre of the Pricaspian basin, the story of the basin changed drastically when its drainage level dropped nearly 1 km in response to the rapid Neogene opening of the South Caspian basin. Rapid fluvial erosion incised deep canyons into Pricaspian sediments and exposed some of the salt diapirs.

3. Mathematical statement of the model problem and numerical approach

3.1. Model assumptions

In modelling salt diapirism we make the following simplifying assumptions. Newtonian rheologies are assumed both for the salt and its overburden. We recognise that most salt overburdens display more complex rheology (e.g., Weijermars et al., 1993). Meanwhile, natural overburdens in a few salt basins exhibit ductile behaviour, for example, the shale and/or impure salt in Central Iran (Jackson et al., 1990, 1995) and the impure Kazanian salt overlying pure Kungurian salt in the Pricaspian basin (Volozh et al., 2003).

We do not consider thermal effects in the modelling, although they may play a significant role in halokinesis (Jackson and Talbot, 1994). No faults can be taken into consideration in the modelling, because our approach is based on the mechanics of continua rather than fracture mechanics. Some of these assumptions are unlikely to be generally valid for salt tectonics, but nevertheless they enable the modelling of deformation in sedimentary basins due to salt movement consistent with geological and geophysical observations.

3.2. Governing equations

We study the problem of advection due to gravity (the slow flow of an incompressible viscous fluid of variable density and viscosity) in the rectangular region $\Omega=(0,x_1=l_1)\times(0,x_2=l_2)\times(0,x_3=l_3)\subset R^3$, where x_1, x_2, and x_3 are the Cartesian coordinates of a spatial point $\mathbf{x}$, and x_3-axis is pointing upward. The following governing equations describe the flow (Ismail-Zadeh et al., 1998, 2001c): momentum conservation

$$\nabla p = \mathrm{div}(\mu\mathbf{E}) + \mathbf{F}, \tag{1}$$

continuity for incompressible fluid

$$\mathrm{div}\mathbf{u} = \partial u_1/\partial x_1 + \partial u_2/\partial x_2 + \partial u_3/\partial x_3 = 0, \tag{2}$$

advection of density and viscosity with the flow

$$\partial\rho/\partial t + \mathbf{u}\bullet\nabla\rho = 0, \qquad \partial\mu/\partial t + \mathbf{u}\bullet\nabla\mu = 0. \tag{3}$$

Eqs. (1)–(3) contain the following variables and parameters: time t; velocity $\mathbf{u}=(u_1(t,\mathbf{x}),\ u_2(t,\mathbf{x}),\ u_3(t,\mathbf{x}))$; pressure $p=p(t,\mathbf{x})$; viscosity $\mu=\mu(t,\mathbf{x})$; and the body force per unit volume $\mathbf{F}=(0,0,-g\rho)$, where g is the acceleration due to gravity, and $\rho=\rho(t,\mathbf{x})$ is density. Here, ∇, div, and $\mathbf{E}$ denote the gradient operator, divergence operator, and strain rate tensor $\mathbf{E}=\{e_{ij}(\mathbf{u})\}=\{\partial u_i/\partial x_j+\partial u_j/\partial x_i\}$, respectively, and

$$\mathrm{div}(\mu\mathbf{E}) = \left(\sum_{m=1}^{3}\frac{\partial(\mu e_{m1})}{\partial x_m}, \qquad \sum_{m=1}^{3}\frac{\partial(\mu e_{m2})}{\partial x_m},\right.$$
$$\left.\sum_{m=1}^{3}\frac{\partial(\mu e_{m3})}{\partial x_m}\right).$$

Eqs. (1)–(3) make up a closed set of equations that determine the unknown $\mathbf{u}$, p, ρ, and μ as functions of independent variables t and $\mathbf{x}$.

The number of unknowns is reduced by introducing the two-component representation of the velocity

potential $\mathbf{\Psi}=(\psi_1, \psi_2, \psi_3=0)$ (Ismail-Zadeh et al., 2001c), from which the velocity is obtained as

$$\mathbf{u} = \text{curl } \mathbf{\Psi}; \ u_1 = -\frac{\partial \psi_2}{\partial x_3}, \ u_2 = \frac{\partial \psi_1}{\partial x_3},$$

$$u_3 = \frac{\partial \psi_2}{\partial x_1} - \frac{\partial \psi_1}{\partial x_2}. \tag{4}$$

Applying the curl operator to Eq. (1) and using the identities curl(∇p)=0, we derive the following equations from Eqs. (1) and (2):

$$D_{2i}(\mu e_{i3}) - D_{3i}(\mu e_{i2}) = gD_2\rho,$$

$$D_{3i}(\mu e_{i1}) - D_{1i}(\mu e_{i3}) = -gD_1\rho,$$

$$D_{1i}(\mu e_{i2}) - D_{2i}(\mu e_{i1}) = 0, \quad i = 1, 2, 3. \tag{5}$$

Hereinafter, we assume a summation over repeated subscripts; $D_j=\partial/\partial x_j$, and $D_{jk}=\partial^2/\partial x_j \partial x_k$, j, k=1, 2, 3. The strain rate components e_{ij} are defined in terms of the vector velocity potential as

$$e_{11} = -2D_{13}\psi_2, \quad e_{22} = 2D_{23}\psi_1,$$
$$e_{33} = 2(D_{31}\psi_2 - D_{32}\psi_1),$$

$$e_{12} = D_{13}\psi_1 - D_{23}\psi_2,$$
$$e_{13} = D_{11}\psi_2 - D_{33}\psi_2 - D_{12}\psi_1,$$

$$e_{23} = D_{33}\psi_1 - D_{22}\psi_1 + D_{21}\psi_2. \tag{6}$$

3.3. Boundary and initial conditions

We set the initial time at zero: t_0=0. On the boundary Γ of Ω, which consists of the faces x_i=0 and x_i=l_i (i=1, 2, 3), we consider three types of boundary conditions: impenetrability with (i) perfect slip or (ii) no-slip conditions, and (iii) lateral penetrability. If a perfect-slip boundary is impenetrable, the velocity vector satisfies the following conditions:

$$\partial \mathbf{u}_\tau / \partial \mathbf{n} = 0, \ \mathbf{u} \cdot \mathbf{n} = 0 \text{ at } \Gamma. \tag{7}$$

Here, $\mathbf{n}$ is the outward unit normal vector at a point on the boundary Γ, and $\mathbf{u}_\tau$ is the projection of the velocity vector onto the tangent plane at the same point on Γ. In the case of a no-slip boundary, the velocity vector satisfies the following condition:

$$\mathbf{u} = 0 \text{ at } \Gamma. \tag{8}$$

And in the case of lateral penetrability, velocity $\mathbf{u}$ satisfies the condition:

$$\mathbf{u} = \mathbf{G}, \quad \mathbf{x} \in \Gamma_*, \quad t \geq t_0, \tag{9}$$

where $\mathbf{G}=(G_1(t,\mathbf{x}),G_2(t,\mathbf{x}),G_3(t,\mathbf{x}))$ is the prescribed function defined at Γ_* (a portion of Γ). The function describes the rate of flow into or out of the model region through Γ_*. At the rest of the boundary $\Gamma \backslash \Gamma_*$ we consider condition (7).

In terms of the vector velocity potential the boundary conditions (7) and (8) take the following forms, respectively:

$$\psi_2 = D_1\psi_1 = D_{11}\psi_2$$
$$= 0 \text{ at } \Gamma_1(x_1 = 0) \text{ and } \Gamma_1(x_1 = l_1),$$

$$\psi_1 = D_2\psi_2 = D_{22}\psi_1$$
$$= 0 \text{ at } \Gamma_2(x_2 = 0) \text{ and } \Gamma_2(x_2 = l_2),$$

$$\psi_1 = \psi_2 = D_{33}\psi_1$$
$$= 0 \text{ at } \Gamma_3(x_3 = 0) \text{ and } \Gamma_3(x_3 = l_3), \tag{10}$$

and

$$\psi_1 = \psi_2 = D_1\psi_2$$
$$= 0 \text{ at } \Gamma_1(x_1 = 0) \text{ and } \Gamma_1(x_1 = l_1),$$

$$\psi_1 = \psi_2 = D_2\psi_1$$
$$= 0 \text{ at } \Gamma_2(x_2 = 0) \text{ and } \Gamma_2(x_2 = l_2),$$

$$\psi_1 = \psi_2 = D_3\psi_1 - D_3\psi_2$$
$$= 0 \text{ at } \Gamma_3(x_3 = 0) \text{ and } \Gamma_3(x_3 = l_3). \tag{11}$$

To solve the direct (forward in time) and inverse (backward in time) problems of gravitational advec-

tion, we assume the density and viscosity to be known at the initial time $t=0$ and at the final (in terms of the direct problem) time $t=\vartheta$, respectively.

Thus, the direct or inverse problem of gravitational advection is to determine functions $\psi_1=\psi_1(t,\mathbf{x})$, $\psi_2=\psi_2(t,\mathbf{x})$, $\rho=\rho(t,\mathbf{x})$, and $\mu=\mu(t,\mathbf{x})$ satisfying Eqs. (3) and (5) in Ω at $t\geq t_0$ (or $t\leq t_0$), prescribed boundary conditions [either Eq. (9), (10) or (11)] and the initial conditions for the direct problem or the final conditions for the inverse problem.

3.4. Numerical approach and its validation

This subsection outlines the numerical method we use in the study. Details of the numerical approach are presented in Appendices A–E.

To solve numerically Eq. (5), we use an Eulerian finite element method (Galerkin method) and replace the equations with an equivalent variational equation (see Appendix A). We represent the components of the vector velocity potential as a sum of tricubic splines ω_{ijk}^s (see Appendix B)

$$\psi_s(t,\mathbf{x}) \approx \psi_{ijk}^s(t)\omega_{ijk}^s(\mathbf{x}), \qquad s = 1, 2 \qquad (12)$$

with unknown functions $\psi_{ijk}^s(t)$. Hereinafter we take i, l, $p=1, 2,\ldots,N_1$; j, m, $q=1, 2,\ldots,N_2$; and k, n, $r=1$, $2,\ldots,N_3$, $s=1, 2$. Density and viscosity are approximated by linear combinations of appropriate trilinear basis functions:

$$\rho(t,\mathbf{x}) \approx \rho_{ijk}(t)\tilde{s}_i^1(x_1)\tilde{s}_j^2(x_2)\tilde{s}_k^3(x_3), \qquad (13)$$

$$\mu(t,\mathbf{x}) \approx \mu_{ijk}(t)\tilde{s}_i^1(x_1)\tilde{s}_j^2(x_2)\tilde{s}_k^3(x_3), \qquad (14)$$

where $\tilde{s}_i^1(x_1)$, $\tilde{s}_j^2(x_2)$, and $\tilde{s}_k^3(x_3)$ are linear basis functions. The trilinear basis functions provide good approximations for step functions (such as density or viscosity that change abruptly from one sedimentary layer to another).

Substituting approximations (12)–(14) into the variational equation we arrive at a system of linear algebraic equations (SLAE) with a positive definite band matrix for the unknown $\psi_{ijk}^s(t)$:

$$\psi_{ijk}^s C_{sijk}^{lmn}\left(\mu_{ijk}\right) = g\rho_{ijk}F_{ijk}^{lmn}, \qquad (15)$$

the coefficients C_{sijk} and F_{ijk} in Eq. (15) are the integrals of various products of cubic splines and their derivatives (see Appendix C). The SLAE is solved by

the conjugate gradient or Seidel iteration methods designed specially for multiprocessor computers (Golub and Van Loan, 1989).

We compute approximations of the density and viscosity for a prescribed velocity by the method of characteristics, i.e., by advecting the initial density and viscosity along the characteristics of Eq. (3) (see Appendix D). A finer grid is used to approximate both density and viscosity as compared to the grid used for computing the vector potential. Therefore, if the values of $\rho_{ijk}(t)$, $\mu_{ijk}(t)$, and $\psi_{ijk}^s(t)$ are known at time t, we calculate these values at time $t+\Delta t$ (see Appendix E).

When we restore salt structures, we replace simply a positive time by a negative time. Such a replacement is possible, because the characteristics of the advection equations (Appendix D) have the same form for both forward and inverse velocity fields (Ismail-Zadeh et al., 2001b).

To check the accuracy of the method we test for: (i) the conservation of mass at each time step and (ii) the accuracy of the vector velocity potential Ψ. We obtain the relative change of mass about 0.1% per 100 time steps (a total number of time steps does not exceed 500 per one run) and consider this error as small enough. Furthermore, we prescribe the right-hand sides in the variational equation as combinations of trigonometric functions, find respective solutions explicitly, and compare them with respective numerical solutions. The relative error for the grid $30\times30\times30$ remains within 0.3%.

4. Model results

In this section we present several models of the evolution of salt structures: (i) salt diapirs evolved from random initial perturbations of the interface between the salt and its overburden (forward and backward models); (ii) an inclined salt layer superimposed on an inclined subsalt layer and partially overlain by two layers of sediments; (iii) salt extrusion and spreading; (iv) a salt diapir complicated by a secondary diapir in the top of its overhang; and (v) a diapir subject to a horizontal flow.

The models were computed on two computational platforms (parallel computers IBM SP2 and MVS-

1000) using 10–16 processors. Although dimensionless values and functions have been used in computations, we represent numerical results in dimensional form. The time step Δt is chosen from the condition that the maximum displacement does not exceed a given small value h, $\Delta t = h/u_{max}$, where u_{max} is the maximum value of the flow velocity.

The rectangular region of all models is divided into $38 \times 38 \times 38$ rectangular elements in order to approximate the vector velocity potential Ψ and viscosity μ [see Eqs. (12) and (14)]. Density ρ [see Eq. (13)] is represented on a grid three times finer, $112 \times 112 \times 112$, and velocity is computed on grid $200 \times 200 \times 200$. Computations of the model problems on 10 processors for one time step take about 100 s on MVS-1000 and about 30 s on IBM SP2.

The model density values are based on estimates of densities of salt and sedimentary rocks in the Pricaspian basin (Nevolin et al., 1977). We treated the viscosity ratio between salt and overburden as the least-known parameter. Because the reference time t_0 is proportional to viscosity μ (that is $t_0 = \mu/\rho g l_3$), the viscosity of the overburden was used as a tuning parameter of our model in order to keep time of model evolution close to observed geological times. The overburden was taken as 10^2 to 10^3 more viscous than salt.

4.1. Model 1. Evolution of salt diapirs and their dynamic restoration

We model a rise of salt diapirs through an overburden deposited prior to the interface perturbation. The model dimensions are $l_1 = l_2 = 30$ km, $l_3 = 10$ km; the viscosities and densities are assumed to be 10^{20} Pa s and 2.65×10^3 kg m^{-3} for the overburden layer and 10^{18} Pa s and 2.24×10^3 kg m^{-3} for salt, respectively.

A salt layer of 3 km thick at the bottom of the model box is overlain by a sedimentary overburden of 7 km thick at time $t=0$. We choose the thicknesses of both salt (see Fig. 1) and its overburden to be consistent with the average thicknesses of equivalent layers in the Pricaspian basin. The interface between the salt and its overburden was disturbed randomly with the amplitude ± 100 m. Fig. 3 (a–d, a front view) and Fig. 4 (a–d, a top view) show the positions of the interface between salt and over-

burden in the model at successive times over a period of about 21 My. The evolution clearly shows two major phases: an initial phase resulting in the development of salt pillows lasting about 18 My (a and b) and a mature phase resulting in salt dome evolution lasting about 3 My (c and d). These results are in agreement with the predictions of a linear analysis and of 2D models of the RT instability (Naimark et al., 1998).

We restore the evolution of salt diapirs predicted by the forward model through successive earlier stages. The final position of the interface between salt and its overburden in the forward model (Figs. 3d and 4d) is used as an initial position of the interfaces for the restoration model. Fig. 3 (d–g) and Fig. 4 (d–g) illustrate successive steps in the restoration of the upbuilt diapirs. We compute least-square errors δ of this restoration using the formula:

$$\delta(x_1, x_2) = \left[\int_0^{l_3} \left(\rho(x_1, x_2, x_3) - \tilde{\rho}(x_1, x_2, x_3) \right)^2 \mathrm{d}x_3 \right]^{1/2},$$

where $\rho(x_1, x_2, x_3)$ is the density at initial time, and $\tilde{\rho}(x_1, x_2, x_3)$ is the restored density (Fig. 4h). The maximum value δ does not exceed 120 kg m^{-3}, and the error is associated with small areas of the initial interface's perturbation.

To demonstrate the stability of the restoration results with respect to changes in the density of the overburden, the restoration procedure was tested by synthetic examples. As in the case of 2D restorations (Ismail-Zadeh et al., 2001b), first we run the forward model for 200 computational time steps (about 30 My). Then we changed the density contrast ($\delta\rho$) between salt and its overburden by a few percents: namely, $\delta\rho$ was chosen to be 400, 405, 410 (the actual contrast), 415, and 420 kg m^{-3}. The evolution of the system was restored for these density contrasts. We found small discrepancies (less than 0.5%) between least square errors for all these test cases. The tests show the solution be stable to small changes in the initial conditions, and this is in agreement with the mathematical theory of well-posed problems (Tikhonov and Samarskii, 1990). Meanwhile, it should be mentioned that if the model is computed for a very long time and the less dense salt layer spreads uniformly into a horizontal layer near the surface, practical restoration of the layered
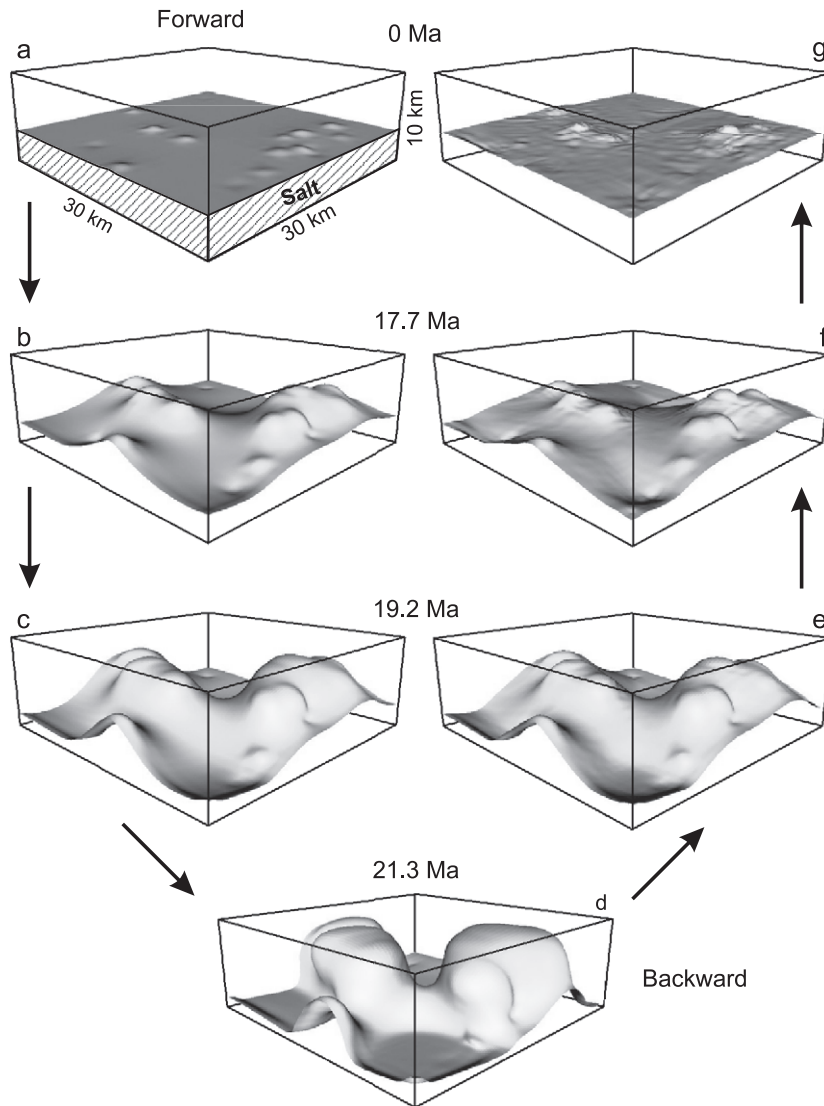
Fig. 3. Evolution (front view) of salt diapirs toward increasing maturity (a–d) and restoration of the evolution (d–g) in model 1. Interfaces between salt and its overburden are presented at successive times. Arrows indicate the flowchart of the figures.

structure becomes impossible (Ismail-Zadeh et al., 2001b).

4.2. Model 2. Evolution of a salt wall

Model 2 represents the evolution of 2D salt walls complicated at a late stage by asymmetric sedimentary loading. The initial geometry of the model is chosen to be 2D (it does not depend on x_2-coordinate). In a model region ($l_1=l_2=20$ km, $l_3=10$ km) we introduce

an inclined salt layer $0.1\ x_1+0.4<x_3<0.05\ x_1+0.6$ of maximum thickness 2 km resting on a subsalt layer. Part of the salt layer was overlain by a pile of sediments on one side of the model (see Fig. 5a): $0.095(x_1-1.0)+0.605<x_3<0.2(x_1-1.0)+0.7$ ($0\le x_1\le l_1$). This sedimentary pile has a wedge-like geometry and maximum thickness 2 km. The viscosity and density are $\mu=10^{21}$ Pa s and $\rho=2.7\times10^3$ kg m^{-3} for the subsalt layer and have the same values for salt and the sedimentary pile as for salt and its overburden in
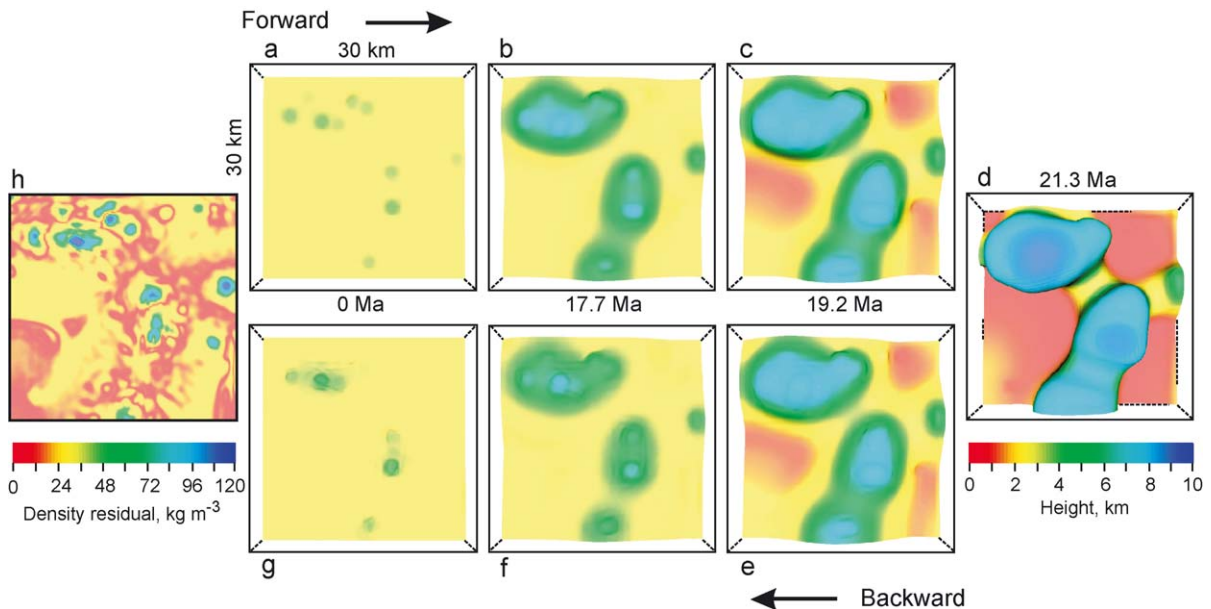
Fig. 4. Evolution (top view) of salt diapirs toward increasing maturity (a–d) and restoration of the evolution (d–g) in model 1 at the same times as in Fig. 3. (h) Restoration errors.

model 1, respectively. The thicknesses of the layers were chosen to be consistent with observations in the Pricaspian basin (Volozh et al., 2003). The configuration of the model is unstable due to lateral asymmetry of the layered structure with respect to gravity. We assumed no sediment erosion or redeposition in the model.

Fig. 5 (b–d) illustrates the growth of a salt wall from the inclined source salt layer over a period of about 8×10^5 y. We then add a new sedimentary load in the corner of the model (see Fig. 5e) and continue our computations for about 1.7 My more. The density and viscosity of the new sediments are the same as for the early pile of sediments. The salt wall increases in relief, as the salt-withdrawal basin fills with the sedimentary overburden (Fig. 5, f–h). The crest of the wall remains at the depositional surface although a thin temporary roof may be thickened by sedimentation or thinned by erosion. Due to the asymmetric loading by sediments at the corner of the model, initially 2D structure is transformed into 3D structures (Fig. 5h). Small salt pillows are evolved from the mature salt wall. The front faces of Fig. 5 (e–h) resemble profiles of centrifuged analogue models simulating the evolu-

tions of salt structures in response to sediment progradation into the Gulf of Mexico (see Figs. 2 and 5–9 in Talbot, 1992).

4.3. Model 3. Salt extrusion and gravity current

Realistic rates of salt extrusion are of major importance to salt tectonics. Late Permian to Jurassic salt extrusions in the southeastern Pricaspian basin and present-day extrusions of salt in the Zagros Mountains of Iran supply natural evidence which allow constraint of numerical models. To analyse the rates at which salt extruded onto the surface and the horizontal velocities at which the gravity current (salt glacier, or namalier) spreads, we model an extrusion of salt and its gravity current spreading over the surface. We consider a salt layer 2 km thick on the bottom of the model region ($l_1=l_2=20$ km, $l_3=10$ km; Fig. 6a) overlain by a sedimentary overburden 6 km thick. The viscosities and densities are 10^{18} Pa s and 2.24×10^3 kg m^{-3} for salt and 10^{21} Pa s and 4.0×10^3 kg m^{-3} for the overburden, respectively. (The density of the overburden is elevated to squeeze the salt from beneath the overburden more rapidly).
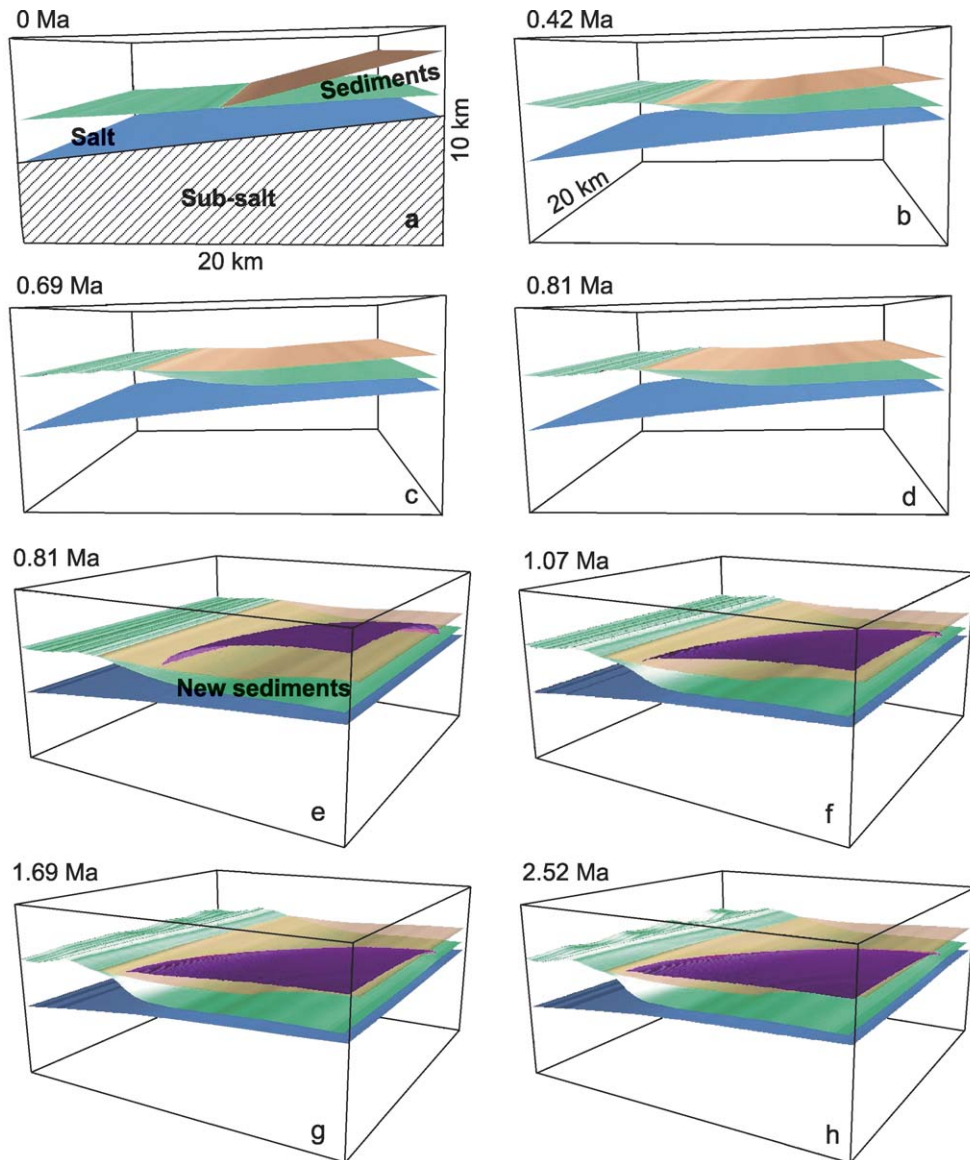
Fig. 5. Evolution (front view) of a salt wall in model 2. At time *t*=0, an inclined salt layer is overlain by sediments at the eastern part of the model region. Later (*t*=0.81 My) a new portion of sediment is added to the structure at the southeastern corner of the model region. Interfaces between salt and subsalt (blue), salt and initial depositional surface (green), the upper surfaces of the first sedimentary pile (brown) and of the second portion of sediments (violet) are presented at successive times.

This model simplifies nature by neglecting dissolution of salt and flow of the salt over a smooth horizontal surface. The salt is extruded on the surface through a pipe-like channel in the overburden with a diameter of 2 km. The channel is filled by salt, and a thin layer of salt (300 m thick) is introduced along the top of the overburden so that the emerging salt spreads over the top surface. Fig. 6 represents front (left panels) and top views (right panels) of the salt extrusion over about 10^5 years. Salt extrudes from the channel as a circular dome. However, the rising salt cannot support its own weight and soon overflows the edges of its orifice and spreads gravitationally away from the centre of the orifice. The dome is soon
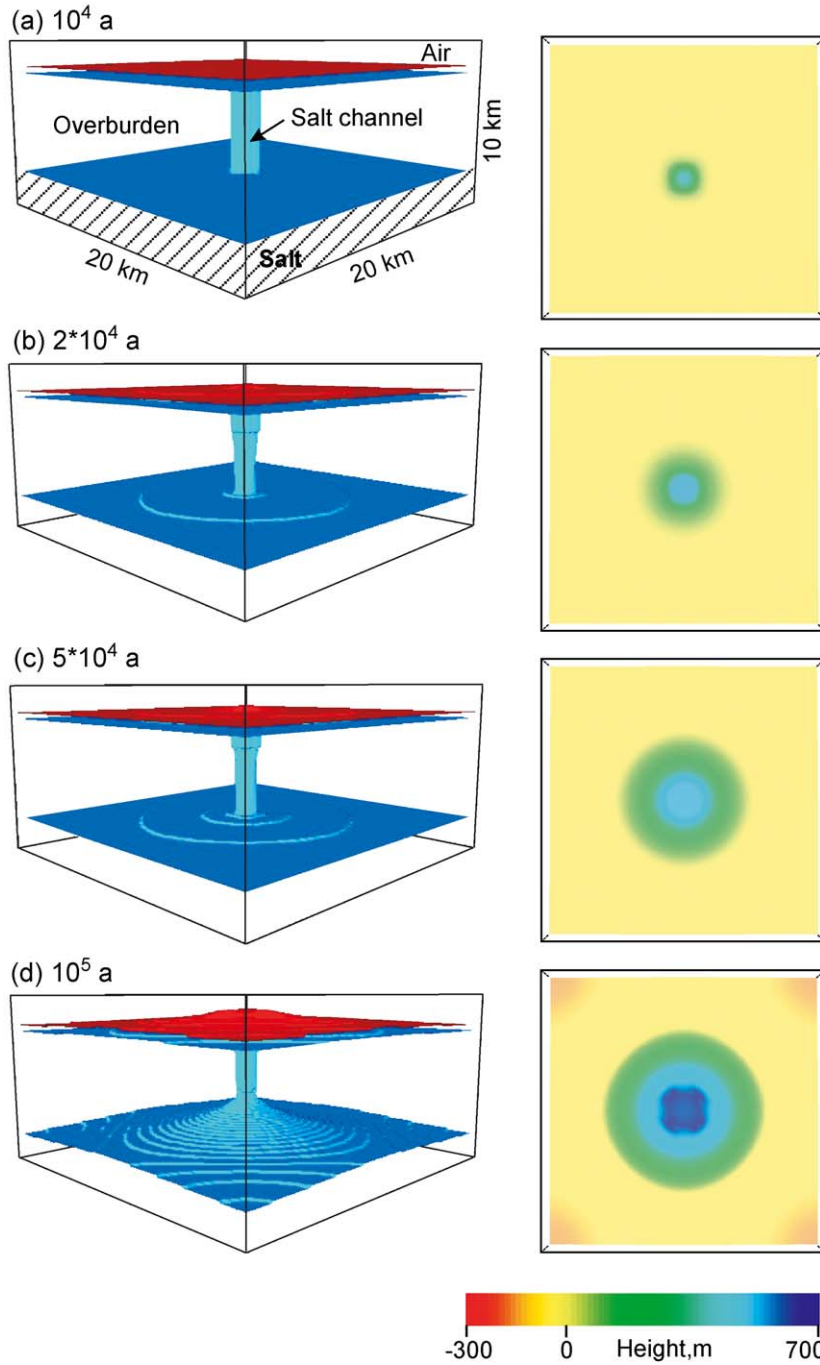
Fig. 6. Extrusion and gravity spreading of salt in model 3. The left panel presents a front view of the model region. A horizontal salt layer at the bottom of the region is overlain by a sedimentary layer (dark blue interface between the layers). Salt escapes from the bottom via the channel (light blue) and extrudes on the depositional surface (red). A thin layer below the depositional surface is salt. The right panel presents a top view of the model region.

surrounded by a plateau or apron of salt (Fig. 6, a–c). The initial vertical rate of salt extrusion predicted by the model is about 10 cm a^{-1} decreasing to about 3 cm a^{-1} in 10^5 years. Meanwhile the rate of gravity spreading, $(u_1^2+u_2^2)^{1/2}$, is about 30 cm a^{-1} near the centre of the dome and about 10 cm a^{-1} at 6 km distance from its centre. The height of the salt dome above the centre of its orifice reaches about 650 m after 10^5 years (Fig. 6d).

4.4. Model 4. Secondary diapirism

The buoyancies of many salt diapirs are sufficiently low that their stiff overburdens have to be faulted and thinned before gravity can drive the rise of reactivate diapir (Vendeville and Jackson, 1992). Faulting of overburdens to salt overhangs can lead to secondary diapirs developing in the top of the salt overhangs.

To simulate this situation, initially we model the growth of a primary salt diapir for 15 My from a small perturbation of the interface between the source salt layer (4 km thick) and its overburden deposited prior to the salt movement. The model region has the following dimensions: $l_1=l_2=30$ km,

$l_3=10$ km. Values of the model parameters are the same as in model 1.

After the source layer has been welded and an overhang has begun to develop, a new horizontal layer of sediments is added above the salt. The interface between the salt overhang and the younger, overlying sediments is then perturbed. This small perturbation gives rise to a secondary diapir (Fig. 7). The density and viscosity of the new sedimentary layer are the same as that of the initial overburden of salt, except for a small cylindrical domain (immediately above the perturbation) inclined at angle 45 to the surface. This domain has a viscosity two orders of magnitude less than that of the surrounding overburden. The perturbation simulates the effect of normal faulting of the overburden by thin-skin extension, and the low viscosity area simulates a fault zone.

Fig. 7 presents four stages of the evolution of the secondary diapir on the top of the primary diapir. The primary diapir develops a mushroom-shaped as its stem thins. Meanwhile the secondary beak-shaped diapir approaches the surface through the cylindrical low viscous domain after displacing most of the thickness of the young sedimentary layer.
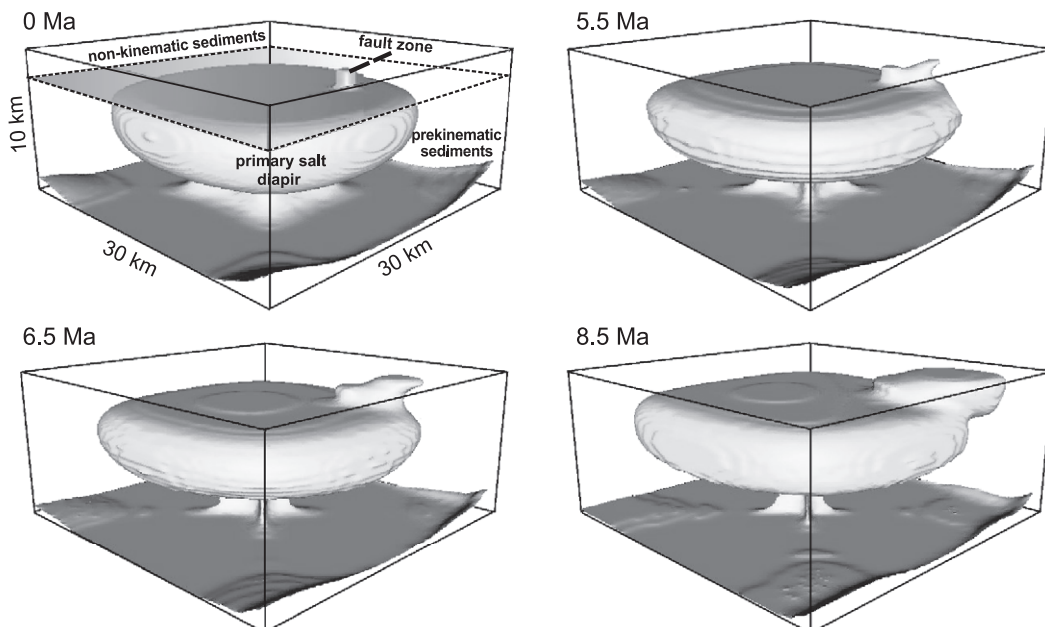

Fig. 7. Evolution of a secondary diapir (model 4) on the top of the primary diapir at successive times.
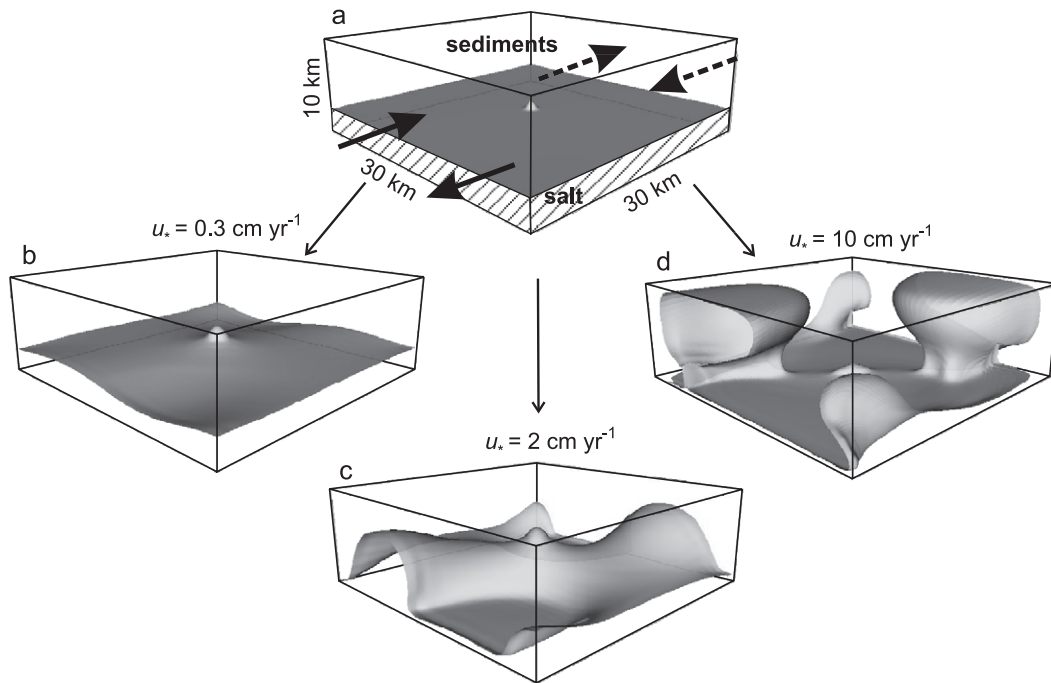
Fig. 8. A salt diapir subject to a lateral flow (model 5). At the initial time the interface between salt and overlain sediments is perturbed in the model's centre (a). The evolved structures (salt/overburden interfaces shown) under the applied horizontal velocity $u_*\sin(2\pi x_2/l_2)$ are presented after 1 My in parts (b), (c), and (d) for three values of u_*.

4.5. Model 5. Evolution of a salt diapir subject to a lateral flow

This subsection presents three models of a salt diapir subject to a lateral flow into and out of the model region ($l_1=l_2=30$ km, $l_3=10$ km). This situation models a growth of salt diapir in a complicated environment, for instance, in regions of heterogeneous extension or shortening. Values of the model parameters are the same as in model 1. A 2.5-km-thick salt layer at the bottom of the model box is overlain initially by a horizontal sedimentary layer 7.5 km thick. The interface between salt and the overburden is subject to a small perturbation (Fig. 8a).

At the two opposed vertical boundaries of the model region $\Gamma_*=\{(x_1,x_2,x_3)\in\bar{\Omega}:\ x_1=0,\ x_1=l_1,\ 0\leq x_2\leq l_2,\ 0\leq x_3\leq l_3\}$ we prescribe an external flow with velocity $\mathbf{u}=(u_1,0,0)$, where $u_1=u_*\sin(2\pi x_2/l_2)$ at $x_2\in[0,l_2]$ and $x_3\in[0,l_3]$, and u_* is a variable model parameter. Both new sediments and underlying salt enter into the model region from its opposite vertical sides and escape from the same sides (see Fig. 8a).

Fig. 8 (b–d) illustrate the evolution of the salt/overburden interface subject to the external horizontal flow after 1 Ma. When the flow rate is sufficiently small (u_*=3 mm year^{-1}, Fig. 8b), the interface changes only slightly compared to a model of diapiric growth with no lateral flow. When the flow rate is chosen to be comparable to the average rate of the diapiric growth (u_*=2 cm year^{-1}, Fig. 8c) and greater than the growth rate by a factor of 5 (u_*=10 cm year^{-1}, Fig. 8d), the evolution of the structure is determined by the lateral flow. The rapid flow results in developing four boundary diapirs (Fig. 8, c and d), which grow much faster than the diapir in the centre of the model region.

5. Discussion

Here we discuss the results of our numerical models and their applicability to the evolution of salt structures in general and to the Pricaspian basin in particular. We should note that the numerical models

in question are not intended to mimic the evolution of any particular salt structures in the Pricaspian basin. Our models are rather phenomenological and simulate the major stages in the evolution of the salt structures in the basin.

Model 1 followed the growth of salt structures upbuilding from small and random initial perturbations in the interface between salt and its prekinematic overburden. Although salt structures in the Pricaspian basin were mainly downbuilt by Triassic to Neogene sediments and the thickness of the overburden varied in time due to sedimentation and erosion, some upbuilt salt structures in the basin might have evolved according to this evolutionary model.

A knowledge of present-day salt structures, based on 3D seismic data, allows reconstructing the history of structural development by removing successively younger layers in turn and restoring older layers and any diapirs to the shapes they were likely to have had at each step. Some salt was extruded and eroded or dissolved in the Pricaspian basin during the major Late Triassic–Early Jurassic hiatus. A restoration of salt structures in such cases is certainly nonunique. To avoid uncertainties concerning the eroded or dissolved volumes of the salt and its overburden, the volumes of salt and overburden were kept constant in model 1, although changes in volumes of salt and/or overburden could be added in modelling.

Permian sediments prograded into the Pricaspian basin from the east, Triassic sediments from the southeast, and Jurassic sediments from the south. Each of these prograding sequences downbuilt successive salt structures basinward from its margins (Volozh et al., 2003). The crests of salt diapirs and salt walls were left near the depositional surface by the superimposed sediments progressively burying (downbuilding) the surrounding salt source layer. Model 2 describes some aspects of this process. The sediments prograded over the inclined salt layer of model 2 downbuilt a 2D salt wall in the east. The later sediments prograded from the southeastern corner converted the 2D salt wall into 3D structures.

Many of the diapirs in Zone R_{4B} of the Pricaspian basin (Fig. 1) have significant overhangs (see Fig. 2e) that can be interpreted as sheets of allochthonous Late Permian salt that extruded over the surface, likely accompanied by some recycling by dissolution and recrystallization. Most Permian salt is likely to

have extruded during an Upper Triassic–Middle Jurassic depositional hiatus, but some was still extruding until the Late Jurassic. Fig. 2e illustrates an example of a salt extrusion with overhangs in the Pricaspian basin. The diapir that extruded this 6 km long sheet of allochthonous salt (probably at the beginning of the Late Triassic) upbuilt through prekinematic Upper Permian and Lower Triassic strata during Middle Triassic deposition in a primary salt-withdrawal basin (Volozh et al., 2003). Lower Jurassic deposition buried the extruded salt. The sheet then sank into a secondary salt-withdrawal basin that migrated distally during periods of active upbuilding of the buoyant salt stock through the surrounding downbuilding sediments. Volozh et al. (2003) consider Iranian salt fountains to be modern examples of many salt structures in the Pricaspian basin as they were in the Upper Permian. Studies of present-day salt extrusions at different stages of development in Iran indicate that, where salt extrudes faster than it dissolves and where deposition of overburden is slow (or absent), extruding salt rises to its level of neutral buoyancy in an extrusive dome that then gravity spreads a sheet of allochthonous salt (Talbot, 1998).

Model 3 has allowed analysis of the rates at which salt can extrude and spread by gravity. The model predicts the average rate of salt extrusion to be about 5 cm a year and the average horizontal velocity of salt spreading to vary between 30 and 10 cm a year. Talbot et al. (2000) estimated an extrusion rate near 1 m a year and horizontal surface velocities measured in the range from 4 to 0.5 m a year for one of the largest salt fountains in Iranian Zagros. These discrepancies between rates of extrusion and spreading can be associated with the order of magnitude difference in viscosity ratio between salt and its overburden used in model 3 and in the model by Talbot et al. (2000). Moreover, the rate of salt spreading (from early vigour to later slowing) depends on the shape of the salt's overburden. An axisymmetric salt flow on a horizontal surface spreads relatively slowly in all directions, although salt extruded over a planar inclined surface would flow in one direction down the inclined substrate much faster.

The faults bounding the polygonal graben system in the Pricaspian basin weakened and thinned the overburden that had onlapped exposed still-potent

Permian–Triassic salt structures. These structures reacted by actively upbuilding back to the depositional surface. Some of these secondary diapir evolved on the top of a salt overhang due to faulting of nonkinematic sediments (see Fig. 2c). In model 4 we have simulated this situation and analysed the growth of primary and secondary diapirs.

It is unlikely that the entirely Pricaspian basin has been subject to large lateral extension or shortening. Nevertheless, some salt structures near the eastern border of the basin might well have been influenced by regional lateral forces. Model 5 explored the effect of lateral forces on the development of salt structure. The shape of a salt diapir is increasingly influenced, if the rate of horizontal flow approaches the average rate of diapiric growth.

6. Conclusion

We opened this multidisciplinary study by presenting our methodology for forward and backward 3D numerical modelling of salt structure dynamics in sedimentary basins. To understand the history of deposition, erosion and deformation in sedimentary basins, tools are needed to restore the basin evolution. The backstripping method that is widely used in basin analysis is severely limited for salt-bearing basins, because the highly mobile and buoyant salt deforms its sedimentary overburden. The suggested numerical technique for backward modeling provides a quantitative tool to study the interaction between sedimentation and salt mobility. In a more comprehensive sense, 3D dynamic restoration of salt structures provides spatial-temporal information on the formation and evolution of structural traps and a general framework for evaluating hydrocarbon migration pathways.

Using the numerical technique we analysed phenomenological (rather then data fitting) models of the evolution of different types of salt structures to better understand salt movements in the Pricaspian basin. Mature salt diapirs developed from an initial random perturbation of the interface between salt and its overburden were restored to their initial stages with small restoration errors. An evolutionary model of a 2D salt wall loaded by a 2D pile of sediments predicted a decomposition of the salt wall into 3D

diapiric structures when a 3D sedimentary wedge was added to the overburden of salt. We estimated rates of salt extrusion (about 5 cm year^{-1}) and gravity current over the depositional surface (10–30 cm year^{-1}) for a reasonable range of physical parameters. We modelled a growth of a secondary diapir initiated by faulting of the overburden to salt overhangs. We showed that the shape of a salt diapir can be very different if the rate of horizontal flow is much greater than the initial rate of diapiric growth solely due to gravity.

We have neglected thermal effects here, although the relevant numerical methodologies have been already developed for modelling the thermomechanical evolution of geostructures, both forwards (Ismail-Zadeh et al., 2001c) and backwards in time (Ismail-Zadeh et al., 2003). The authors work on the problem of combined structural and thermal restorations of salt basins.

The numerical methodology and models developed here allow the following conclusions:

(i)   The suggested numerical approach is appropriate for modelling of the evolution of salt structures in salt-bearing basins where the salt overburden is essentially ductile.

(ii) The three-dimensional backward modelling technique can be used to restore salt structures and their overburden to their earlier depositional steps.

(iii) The different sizes, shapes and maturities of salt structures in different parts of the Pricaspian basin reflect areal differences in thicknesses of salt and its overburden and loading history.

Appendix A. The variational equation

To apply the Galerkin method to Eq. (5), we replace the equations with an equivalent variational equation. Consider any arbitrary admissible test vector function $\mathbf{\Phi}=(\varphi_1,\varphi_2,0)$ satisfying the same conditions as for the vector function $\mathbf{\Psi}$ and multiply the first two equations of Eq. (5) by φ_1 and φ_2, respectively. Integrating by parts the obtained equations over Ω and using the boundary conditions for the desired and test vector functions, we obtain the variational equation

$$L(\mu;\mathbf{\Psi},\mathbf{\Phi}) = R(\mu,\rho;\mathbf{\Phi}), \qquad (A1.1)$$

where

$$L(\mu;\mathbf{\Psi},\mathbf{\Phi}) = \int_\Omega \mu[2e_{11}\tilde{e}_{11} + 2e_{22}\tilde{e}_{22} + 2e_{33}\tilde{e}_{33} \\ + e_{12}\tilde{e}_{12} + e_{13}\tilde{e}_{13} + e_{23}\tilde{e}_{23}]d\mathbf{x},$$

and the expressions for $\tilde{e}_{ij}$ in terms of $\mathbf{\Phi}$ are identical to the expressions for e_{ij} in terms of $\mathbf{\Psi}$. The right-hand side of Eq. (A1.1) has the following forms: in the case of condition (9) (Tsepelev et al., 2001)

$$R(\mu,\rho;\mathbf{\Phi}) = \int_\Omega g\rho\left(\frac{\partial\phi_1}{\partial x_2} - \frac{\partial\phi_2}{\partial x_1}\right)d\mathbf{x}$$
$$+ \int_{\Gamma_1(x_1=l_1)} \mu[e_{12}G_2 + e_{13}G_3]d\Gamma$$
$$- \int_{\Gamma_1(x_1=0)} \mu[e_{12}G_2 + e_{13}G_3]d\Gamma$$
$$+ \int_{\Gamma_2(x_2=l_2)} \mu[e_{21}G_1 + e_{23}G_3]d\Gamma$$
$$- \int_{\Gamma_2(x_2=0)} \mu[e_{21}G_1 + e_{23}G_3]d\Gamma$$
$$+ \int_{\Gamma_3(x_3=l_3)} \mu[e_{31}G_1 + e_{32}G_2]d\Gamma$$
$$- \int_{\Gamma_3(x_3=0)} \mu[e_{31}G_1 + e_{32}G_2]d\Gamma,$$

and in the case of conditions (10) and (11)

$$R(\mu,\rho;\mathbf{\Phi}) = \int_\Omega g\rho\left(\frac{\partial\phi_1}{\partial x_2} - \frac{\partial\phi_2}{\partial x_1}\right)d\mathbf{x}.$$

Appendix B. Tricubic basis splines

The functions to be found are represented as sums of tricubic basis splines with unknown coefficients. Tricubic basis splines are products of basis cubic splines constructed in the following manner. A segment $0\leq y\leq L$ is divided into N small segments by points $y_n=(n-1)h$, $h=L/(N-1)$, $n=1, 2,\ldots,N$. Let us introduce seven functions: $\alpha(y)$, $\beta(y)$, $\delta(y)$, $\delta^*(y)$, $\beta^*(y)$, and $\alpha^*(y)$ defined for $0\leq y\leq 3h$ and $\gamma(y)$ defined for $0\leq y\leq 4h$, each being a cubic $c_0+c_1(y-y_i)/h+c_2((y-y_i)/h)^2+c_3((y-y_i)/h)^3$ in a small segment $y_{n-1}\leq y\leq y_n$, $n=1, 2, 3, 4$.

These seven standard functions so defined have the following properties. These functions and their first and second derivatives are continuous over their supports, so that these functions are splines. They satisfy the following conditions:

at $y = 0$: $\alpha(y) = \beta(y) = \beta^*(y) = \alpha^*(y)$
$= \delta^*(y) = 0, \delta(y) = 1,$
$\alpha'(y) = \delta'(y) = \beta^{*\prime}(y) = \alpha^{*\prime}(y)$
$= \delta^{*\prime}(y) = 0, \beta'(y) = 1/h,$
$\beta''(y) = \delta''(y) = \beta^{*\prime\prime}(y) = \alpha^{*\prime\prime}(y)$
$= \delta^{*\prime\prime}(y) = 0, \alpha''(y) = 1/h^2,$

at $y = 3h$: $\alpha(y) = \beta(y) = \gamma(y) = \beta^*(y) = \alpha^*(y)$
$= \delta(y) = 0, \delta^*(y) = 1,$
$\alpha'(y) = \delta'(y) = \gamma'(y) = \beta'(y) = \alpha^{*\prime}(y)$
$= \delta^{*\prime}(y) = 0, \beta^{*\prime}(y) = -1/h,$
$\beta''(y) = \delta''(y) = \gamma''(y) = \beta^{*\prime\prime}(y) = \alpha''(y)$
$= \delta^{*\prime\prime}(y) = 0, \alpha^{*\prime\prime}(y) = 1/h^2,$

at $y = 4h$: $\gamma(y) = \gamma'(y) = \gamma''(y) = 0,$

at $y = 2h$: $\gamma(y) = 1.$

Basis splines on the interval $0 \leq y \leq L$ are functions $s_1(y)$, $s_2(y), \ldots, s_N(y)$ chosen from the above standard splines:

$s_1(y)$ and $s_2(y)$ (boundary splines) are selected from $\alpha(y)$, $\beta(y)$, $\delta(y)$ to satisfy boundary conditions at $y=0$, e.g., $s_1(y) = \delta(y)$ and $s_2(y) = \beta(y)$ to approximate a function $f(y)$ such that $f(0) = a$ and $f''(0) = 0$;

$s_{N-1}(y)$ and $s_N(y)$ (boundary splines) are selected from $\alpha^*(y)$, $\beta^*(y)$, $\delta^*(y)$ to satisfy boundary conditions at $y=L$ in the same manner as at $y=0$;

$$s_i(y) = \gamma(y - (i-2)h) \text{ for } (i-2)h \leq y \leq (i+2)h,$$
$$i = 2, 3, \ldots, N-2.$$

Tricubic basis splines have the form $\omega_{ijk}(x_1, x_2, x_3) = \eta_i(x_1)\zeta_j(x_2)\vartheta_k(x_3)$ where $\eta_i(x_1)$, $\zeta_j(x_2)$, and $\vartheta_k(x_3)$ are basis splines constructed similarly to $s_i(y)$ over segments $0 \leq x_1 \leq l_1$, $0 \leq x_2 \leq l_2$, and $0 \leq x_3 \leq l_3$ (edges of Ω), divided into N_1, N_2, and N_3 small segments of length h_1, h_2, and h_3, respectively. Boundary splines in $\eta_i(x_1)$, $\zeta_j(x_2)$, and $\vartheta_k(x_3)$ are selected is such a way as to satisfy boundary conditions of the problem.

Appendix C. Coefficients in the discrete governing equations

Here we present coefficients entering into Eq. (15). The matrix in the equation takes the form

$$C_{sijk}^{lmn} = \sum \mu_{pqr} w_{a_1 a_2 b_1 b_2 c_1 c_2} A_{silp}^{a_1 a_2} B_{sjmq}^{b_1 b_2} C_{sknr}^{c_1 c_2},$$

where the sum is taken over all nonnegative integers a_1, a_2, b_1, b_2, c_1, and c_2 such that each of them does not exceed 2 and $a_1 + a_2 + b_1 + b_2 + c_1 + c_2 = 4$. The values of $w_{a_1 a_2 b_1 b_2 c_1 c_2}$ are readily obtained by collecting similar terms in the sums. Coefficients $A_{silp}^{a_1 a_2}$, $B_{sjmq}^{b_1 b_2}$, and $C_{sknr}^{c_1 c_2}$ are integrals of the form

$$A_{silp}^{a_1 a_2} = \int_0^{L_1} \left(D_{a_1} \eta_i^s(x_1) \right) \left(D_{a_2} \eta_l^s(x_1) \right) \tilde{s}_p^1(x_1) \mathrm{d}x_1,$$

$$B_{sjmq}^{b_1 b_2} = \int_0^{L_2} \left(D_{b_1} \zeta_j^s(x_2) \right) \left(D_{b_2} \zeta_m^s(x_2) \right) \tilde{s}_q^2(x_2) \mathrm{d}x_2,$$

$$C_{sknr}^{c_1 c_2} = \int_0^{L_3} \left(D_{c_1} \vartheta_k^s(x_3) \right) \left(D_{c_2} \vartheta_n^s(x_3) \right) \tilde{s}_r^1(x_3) \mathrm{d}x_3,$$

where $\{\eta\}$, $\{\zeta\}$, and $\{\vartheta\}$ are cubic basis splines (see Appendix B) and $\{\tilde{s}\}$ are linear basis functions. Coefficients F_{ijk}^{lmn} take the following forms:

$$F_{ijk}^{lmn} = P_{il}^{01} Q_{jm}^{00} R_{kn}^{00} - P_{il}^{00} Q_{jm}^{01} R_{kn}^{00},$$

where

$$P_{il}^{ab} = \int_0^{L_1} \left(D_a \tilde{s}_i^1(x_1) \right) \left(D_b \eta_l^1(x_1) \right) \mathrm{d}x_1,$$

$$Q_{jm}^{ab} = \int_0^{L_2} \left(D_a \tilde{s}_j^2(x_2) \right) \left(D_b \zeta_m^1(x_2) \right) \mathrm{d}x_2,$$

$$R_{kn}^{ab} = \int_0^{L_3} \left(D_a \tilde{s}_k^3(x_3) \right) \left(D_b \vartheta_n^1(x_3) \right) \mathrm{d}x_3.$$

Appendix D. Method of characteristics

The method of characteristics can be used in computations with relatively small numerical diffusion of density and viscosity (Marchuk, 1994). The characteristics of advection equations are defined as

$$\mathrm{d}\mathbf{x}(t)/\mathrm{d}t = \mathbf{u}(t, \mathbf{x}(t)). \qquad (A4.1)$$

The density and viscosity have constant values on the characteristics:

$$\rho(t, \mathbf{x}(t)) = \rho_0(\mathbf{x}(t_0)), \mu(t, \mathbf{x}(t)) = \mu_0(\mathbf{x}(t_0)), \qquad t \geq 0.$$

Provided that the velocity has already been computed at time t, we find the characteristics at time $t - \Delta t$ using the Euler formula:

$$\mathbf{x}(t - \Delta t) \approx \mathbf{x}(t) - \Delta t \mathbf{u}(t, \mathbf{x}(t)).$$

The latter relations are used to define density and viscosity in Ω at $t > 0$:

$$\rho(t, \mathbf{x}) \approx \rho(t - \Delta t, \mathbf{x} - \Delta t \mathbf{u}(t, \mathbf{x})),$$
$$\mu(t, \mathbf{x}) \approx \mu(t - \Delta t, \mathbf{x} - \Delta t \mathbf{u}(t, \mathbf{x})).$$

When trilinear basis functions are used to approximate density and viscosity, a sufficiently large number of independent modules can be organised to compute the characteristics of advection equations and the corre-

sponding densities and viscosities at parallel computers with a distributed memory (Ismail-Zadeh et al., 2001c).

Appendix E. Computational procedure

Here we describe briefly the procedure for solving the problem. A uniform discretisation of the time axis, $t_n = t_0 + \tau n$ $(n \in Z)$, is defined a priori, where τ is the grid parameter. Next, computations are organised in which n is consecutively assigned integer values ranging from 0 to m. The integer m is prescribed prior to computations to set the length of the interval $[t_0, t_m]$ of integration. When necessary, the process can be continued further, starting from t_m as an initial time. At each iteration step in time, the following principal steps are computed sequentially.

Step 1.   The density $\rho = \rho(t_n, \cdot)$ and viscosity $\mu = \mu(t_n, \cdot)$ at $t = t_n$ are used to determine the components of vector velocity potential $\mathbf{\Psi} = \mathbf{\Psi}(t_n, \cdot)$. To solve Eq. (15), we compute the matrix C_{sijk}^{lmn}, then the right-hand side $g \rho_{ijk}(t) F_{ijk}^{lmn}$, and find unknowns $\psi_{ijk}^s(t)$ at $t = t_n$.
Step 2.   Eq. (4) is used to calculate the components of velocity $\mathbf{u} = \mathbf{u}(t_n, \cdot)$.
Step 3.   The characteristics $\mathbf{x}(t_n)$ of the advection equations are found from Eq. (A4.1).
Step 4.   The density and viscosity are advected along the characteristics. The velocity $\mathbf{u} = \mathbf{u}(t_n, \cdot)$, characteristics $\mathbf{x}(t_n)$, density $\rho = \rho(t_n, \cdot)$, and viscosity $\mu = \mu(t_n, \cdot)$ are used to compute new density $\rho = \rho(t_{n+1}, \cdot)$ and viscosity $\mu = \mu(t_{n+1}, \cdot)$, at $t = t_{n+1}$ by solving Eq. (18).

The process results in a set of components of the vector velocity potential $\mathbf{\Psi} = \mathbf{\Psi}(t_n, \cdot)$, velocity $\mathbf{u} = \mathbf{u}(t_n, \cdot)$, density $\rho = \rho(t_n, \cdot)$ and viscosity $\mu = \mu(t_n, \cdot)$ at $t = t_n$ $(n = 0, \ldots, m)$. Once these distributions are available, the evolution of the system on the interval $[t_0, t_m]$ can be recovered in more detail by interpolation.

References

Biot, M.A., Odé, H., 1965. Theory of gravity instability with variable overburden and compaction. Geophysics 30 (2), 213–227.

Chandrasekhar, S., 1961. Hydrodynamic and Hydromagnetic Stability, 2nd ed. Oxford University Press. 654 pp.

Conrad, C.P., Molnar, P., 1997. The growth of Rayleigh–Taylor instability in the lithosphere for various rheological and density structures. Geophysical Journal International 129, 95–112.

Daudré, B., Cloetingh, S., 1994. Numerical modelling of salt diapirism: influence of the tectonic regime. Tectonophysics 240, 59–79.

Golub, G.H., Van Loan, C.F., 1989. Matrix Computations, 2nd ed. Johns Hopkins, Baltimore. 476 pp.

Ismail-Zadeh, A.T., Korotkii, A.I., Naimark, B.M., Suetov, A.P., Tsepelev, I.A., 1998. Implementation of a three-dimensional hydrodynamic model for evolution of sedimentary basins. Computational Mathematics and Mathematical Physics 38 (7), 1138–1151.

Ismail-Zadeh, A.T., Tsepelev, I.A., Talbot, C.J., Oster, P., 2000. A numerical method and parallel algorithm for three-dimensional modeling of salt diapirism. In: Keilis-Borok, V.I., Molchan, G.M. (Eds.), Problems in Dynamics and Seismicity of the Earth. GEOS, Moscow, pp. 62–76.

Ismail-Zadeh, A.T., Huppert, H.E., Lister, J.R., 2001a. Analytical modelling of viscous diapirism through a strongly non-Newtonian overburden subject to horizontal forces. Journal of Geodynamics 31, 447–458.

Ismail-Zadeh, A.T., Talbot, C.J., Volozh, Y.A., 2001b. Dynamic restoration of profiles across diapiric salt structures: numerical approach and its applications. Tectonophysics 337, 21–36.

Ismail-Zadeh, A.T., Korotkii, A.I., Naimark, B.M., Tsepelev, I.A., 2001c. Numerical simulation of three-dimensional viscous flow with gravitational and thermal effects. Computational Mathematics and Mathematical Physics 41 (9), 1331–1345.

Ismail-Zadeh, A.T., Huppert, H.E., Lister, J.R., 2002. Gravitational and buckling instabilities of a rheologically layered structure: implications for salt diapirism. Geophysical Journal International 148 (2), 288–302.

Ismail-Zadeh, A.T., Korotkii, A.I., Naimark, B.M., Tsepelev, I.A., 2003. Three-dimensional numerical simulation of the inverse problem of thermal convection. Computational Mathematics and Mathematical Physics 43 (4), 587–599.

Jackson, M.P.A., 1995. Retrospective salt tectonics. In: Jackson, M.P.A., Roberts, D.G., Snelson, S. (Eds.), Salt Tectonics—A Global Perspective, Memoir, vol. 65. American Association of Petroleum Geologists, Tulsa, pp. 1–28.

Jackson, M.P.A., Talbot, C.J., 1994. Advances in salt tectonics. In: Hancock, P.L. (Ed.), Continental Deformation. Pergamon Press, Oxford, pp. 159–179.

Jackson, M.P.A., Talbot, C.J., Cornelius, R.R., 1988. Centrifuge modelling of the effects of aggradation and progradation on syn-depositional salt structures. Report of Investigations, vol. 173. Bureau of Economic Geology, University of Texas, Austin. 93 pp.

Jackson, M.P.A., Cornelius, R.R., Craig, C.H., Gansser, A., Stöcklin, J., Talbot, C.J., 1990. Salt diapirs of the Great Kavir, central Iran. Memoir, vol. 177. Geological Society of America. 139 pp.

Jackson, M.P.A., Vendeville, B.C., Schultz-Ela, D.D., 1994. Structural dynamics of salt systems. Annual Review of Earth and Planetary Sciences 22, 93–117.

Jackson, M.P.A., Roberts, D.G., Snelson, S., 1995. Salt Tectonics—A Global Perspective, Memoir, vol. 65. American Association of Petroleum Geologists, Tulsa.

Kaus, B.J.P., Podladchikov, Y.Y., 2001. Forward and reverse modeling of the three-dimensional viscous Rayleigh–Taylor instability. Geophysical Research Letters 28, 1095–1098.

Korotkii, A.I., Tsepelev, I.A., Ismail-Zadeh, A.T., Naimark, B.M., 2002. Three-dimensional backward modeling in problems of Rayleigh–Taylor instability. Izvestiya/Proceedings of the Ural State University 22 (4), 96–104.

Koyi, H., 1996. Salt flow by aggrading and prograding overburdens. In: Alsop, I., Blundell, D., Davison, I. (Eds.), Salt Tectonics, Geological Society Special Publication, vol. 100, pp. 243–258. London.

Koyi, H., 1997. Analogue modelling; from a qualitative to a quantitative technique, a historical outline. Journal of Petroleum Geology 20 (2), 223–238.

Marchuk, G.I., 1994. Numerical Methods and Applications. CRC Press, Boca Raton. 272 pp.

Naimark, B.M., Ismail-Zadeh, A.T., 1989. Gravitational instability of a layered medium with Maxwell rheology. Proceedings of the USSR Academy of Sciences, Physics of the Earth 25 (12), 998–1004.

Naimark, B.M., Ismail-Zadeh, A.T., Jacoby, W.R., 1998. Numerical approach to problems of gravitational instability of geostructures with advected material boundaries. Geophysical Journal International 134, 473–483.

Nevolin, N.B., Kunin, N.Ya., Andreev, A.P., Volozh, Yu.A., 1977. Based on Geophysical Data Geological Structure and Oil–gas Content of Intracratonic Salt Basins (in Russian). Nedra, Moscow. 233 pp.

Poliakov, A.N.B., van Balen, R., Podladchikov, Yu., Daudré, B., Cloetingh, S., Talbot, C., 1993a. Numerical analysis of how sedimentation and redistribution of surficial sediments affects salt diapirism. Tectonophysics 226, 199–216.

Poliakov, A.N.B., Podladchikov, Yu., Talbot, C., 1993b. Initiation of salt diapirs with frictional overburdens: numerical experiments. Tectonophysics 228, 199–210.

Poliakov, A., Podladchikov, Yu., Dawson, E., Talbot, C., 1996. Salt diapirism with simultaneous brittle faulting and viscous flow. In: Alsop, I., Blundell, D., Davison, I. (Eds.), Salt Tectonics, Geological Society Special Publication, vol. 100, pp. 291–302. London.

Price, N.J., 1966. Fault and Joint Development in Brittle and Semi-Brittle Rock. Pergamon Press, Oxford. 216 pp.

Ramberg, H., 1968. Instability of layered system in the field of gravity. Physics of the Earth and Planetary Interiors 1, 427–474.

Römer, M.-M., Neugebauer, H.J., 1991. The salt dome problem: a multilayered approach. Journal of Geophysical Research 96, 2389–2396.

Schmeling, H., 1987. On the relation between initial conditions and late stages of Rayleigh–Taylor instabilities. Tectonophysics 133, 65–80.

Talbot, C.J., 1977. Inclined and asymmetric upward-moving gravity structures. Tectonophysics 42, 159–181.

Talbot, C.J., 1992. Centrifuged models of Gulf of Mexico profiles. Marine and Petroleum Geology 9, 412–432.

Talbot, C.J., 1995. Molding of salt diapirs by stiff overburdens. In: Jackson, M.P.A., Roberts, D.G., Snelson, S. (Eds.), Salt Tectonics—A Global Perspective, Memoir, vol. 65. American Association of Petroleum Geologists, Tulsa, pp. 61–75.

Talbot, C.J., 1998. Extrusion of Hormuz salt in Iran. In: Blundell, D.J., Scott, A.C. (Eds.), Lyell: The Past is the Key to the Present, Special Publication, vol. 143. Geological Society, London, pp. 315–334.

Talbot, C.J., Jackson, M.P.A., 1987. Internal dynamics and kinematics of salt structures. American Association of Petroleum Geologist Bulletin 71, 1068–1093.

Talbot, C.J., Jarvis, R.J., 1984. Age, budget and dynamics of an active salt extrusion in Iran. Journal of Structural Geology 6, 521–524.

Talbot, C.J., Rönnlund, P., Schmeling, H., Koyi, H., Jackson, M.P.A., 1991. Diapiric spoke patterns. Tectonophysics 188, 187–201.

Talbot, C.J., Medvedev, S., Alavi, M., Shahrivar, H., Heidari, E., 2000. Salt extrusion at Kuh-e-Jahani, Iran, from June 1994 to November 1997. In: Vendeville, B., Mart, Y., Vigneresse, J.-L. (Eds.), Salt, Shale and Igneous Diapirs in and Around Europe, Special Publications, vol. 174. Geological Society, London, pp. 93–110.

Tikhonov, A.N., Samarskii, A.A., 1990. Equations of Mathematical Physics. Dover Publications, New York. 765 pp.

Tsepelev, I.A., Korotkii, A.I., Ismail-Zadeh, A.T., 2001. Parallel algorithms for modeling of Rayleigh–Taylor instability of geostructures subject to horizontal forces (in Russian). In: Ulianov, O.N. (ed.) Algorithms and Software for Parallel Computations. Institute of Mathematics and Mechanics, Ural Branch of the Russian Academy of Sciences, Ekaterinburg, pp. 275–286.

van Keken, P.E., Spiers, C.J., van den Berg, A.P., Muyzert, E.J., 1993. The effective viscosity of rocksalt: implementation of steady-state creep laws in numerical models of salt diapirism. Tectonophysics 225, 457–476.

Vendeville, B.C., Jackson, M.P.A., 1992. The rise of diapirs during thin-skinned extension. Marine and Petroleum Geology 9, 331–353.

Volozh, Y.A., 1991, Seismostratigraphic analysis of sedimentary basins of the western Kazakhstan, D.Sc. dissertation, Institute of Geology, Russian Academy of Sciences, Moscow, 49 pp. (in Russian).

Volozh, Y.A., Talbot, C.J., Ismail-Zadeh, A.T., 2003. Salt structures and hydrocarbons in the Pricaspian basin. American Association of Petroleum Geologist Bulletin 87 (2), 313–334.

Weijermars, R., Jackson, M.P.A., Vendeville, B., 1993. Rheological and tectonic modeling of salt provinces. Tectonophysics 217, 143–174.

Woidt, W.-D., 1978. Finite element calculations applied to salt dome analysis. Tectonophysics 50, 369–386.